

INFRARED H₃⁺ AND CO STUDIES OF THE GALACTIC CORE: GCIRS 3 AND GCIRS 1W¹

MIWA GOTO², T. R. GEBALLE³, NICK INDRIOLO⁴, FARHAD YUSEF-ZADEH⁵, TOMONORI USUDA⁶, THOMAS HENNING⁷, AND
TAKESHI OKA⁸

Draft version April 10, 2014

ABSTRACT

We have obtained improved spectra of key fundamental band lines of H₃⁺, $R(1,1)^l$, $R(3,3)^l$, and $R(2,2)^l$, and ro-vibrational transitions of CO on sightlines toward the luminous infrared sources GCIRS 3 and GCIRS 1W, each located in the Central Cluster of the Galactic center within several arcseconds of Sgr A*. The spectra reveal absorption occurring in three kinds of gaseous environments: (1) cold dense and diffuse gas associated with foreground spiral/lateral arms; (2) warm and diffuse gas absorbing over a wide and mostly negative velocity range, which appears to fill a significant fraction of the Galaxy's Central Molecular Zone (CMZ); and (3) warm, dense and compact clouds with velocities near +50 km s⁻¹ probably within 1-2 pc of the center. The absorptions by the first two cloud types are nearly identical for all the sources in the Central Cluster, and are similar to those previously observed on sightlines from Sgr A* to 30 pc east of it. Cloud type (3), which has only been observed toward the Central Cluster, shows distinct differences between the sightlines to GCIRS 3 and GCIRS 1W, which are separated on the sky by only 0.33 pc in projection. We identify this material as part of an inward extension of the Circumnuclear Disk previously known from HCN mapping. Lower limits on the products of the hydrogen ionization rate ζ and the path length L are 2.3×10^5 cm s⁻¹ and 1.5×10^3 cm s⁻¹ for the warm and diffuse CMZ gas and for the warm and dense clouds in the core, respectively. The limits indicate that the ionization rates in these regions are well above 10^{-15} s⁻¹.

Subject headings: Galaxy: center — ISM: clouds — ISM: lines and bands — ISM: molecules — stars: individual (GCIRS 1W, GCIRS 3)

1. INTRODUCTION

Detailed knowledge of the gaseous environment in the Galactic center (GC) is of vital importance in understanding the wide range of extraordinary phenomena that have recently taken place and are currently taking place there. For several decades many well-known atomic and molecular species have been used as probes to help characterize that environment. In the last decade, a newly discovered species, H₃⁺, found in interstellar clouds eighteen years ago (Geballe & Oka 1996) and towards the Galactic center one year later (Geballe et al. 1999), has

proven to be a unique and valuable tool in this endeavor.

The simple chemistry of H₃⁺, i.e., its production through ionization of H₂ (mainly either by cosmic rays or X-rays) followed by the rapid proton hop reaction $H_2 + H_2^+ \rightarrow H_3^+ + H$ and its destruction, in diffuse clouds by recombination with electrons $H_3^+ + e \rightarrow H + H + H$ or $H + H_2$ and in dense clouds by reaction primarily with CO, allows one to reliably determine the product ζL , where L is line of sight dimension of the cloud, and ζ is the ionization rate of H₂. In addition, column densities of H₃⁺ in its low rotational levels are useful for measuring the temperature T and number density n of the gas (Oka & Epp 2004; Oka et al. 2005; Oka 2006).

Previous studies of H₃⁺ in the GC have revealed the presence there of a vast amount of warm ($T \sim 250$ K) and diffuse ($n \leq 100$ cm⁻³) gas (Oka et al. 2005; Goto et al. 2008) and an unusually high ionization rate, on the order of $\zeta \sim 10^{-15}$ s⁻¹. The presence of so much H₃⁺ requires a drastic change in our understanding of the physical states and volume filling factors of the gas in the Central Molecular Zone (CMZ, Morris & Serabyn 1996; Lazio & Cordes 1998), the name given to the region of radius ~ 200 pc at the center. The high ionization rate required to account for the large column density of H₃⁺ is potentially important for understanding the overall energetics of the Galactic center. A high ionization fraction and an elevated gas temperature (e.g., Morris et al. 1983), much higher than the dust temperature of ~ 20 K (Pierce-Price et al. 2000; Lis et al. 2001), also may be consistent with the cosmic rays being the dominant heating source for the gas (Güsten, Walmsley, & Pauls

mgoto@usm.lmu.de

¹ Based on data collected during the CRIRES Science Verification program (60.7A-9057) and open time program (079.C-0874) at the VLT on Cerro Paranal (Chile), which is operated by the European Southern Observatory (ESO). Based also on data collected at Subaru Telescope, which is operated by the National Astronomical Observatory of Japan. Based on data obtained from the ESO Science Archive Facility under request number MGOTO 43308.

² Universitäts-Sternwarte München, Scheinerstr. 1, D-81679 Munich, Germany; mgoto@usm.lmu.de.

³ Gemini Observatory, 670 North A'ohoku Place, Hilo, HI 96720; tgeballe@gemini.edu

⁴ Department of Physics and Astronomy, Johns Hopkins University, 3400 N. Charles St., Baltimore, MD 21218; indriolo@pha.jhu.edu.

⁵ Department of Physics and Astronomy, Northwestern University, Evanston, IL 60208; zadeh@northwestern.edu.

⁶ Subaru Telescope, 650 North A'ohoku Place, Hilo, HI 96720; usuda@naoj.org.

⁷ Max-Planck-Institut für Astronomie, Königstuhl 17, D-69117 Heidelberg, Germany; henning@mpia.de.

⁸ Department of Astronomy and Astrophysics, Department of Chemistry, and Enrico Fermi Institute, University of Chicago, Chicago, IL 60637; t-oka@uchicago.edu

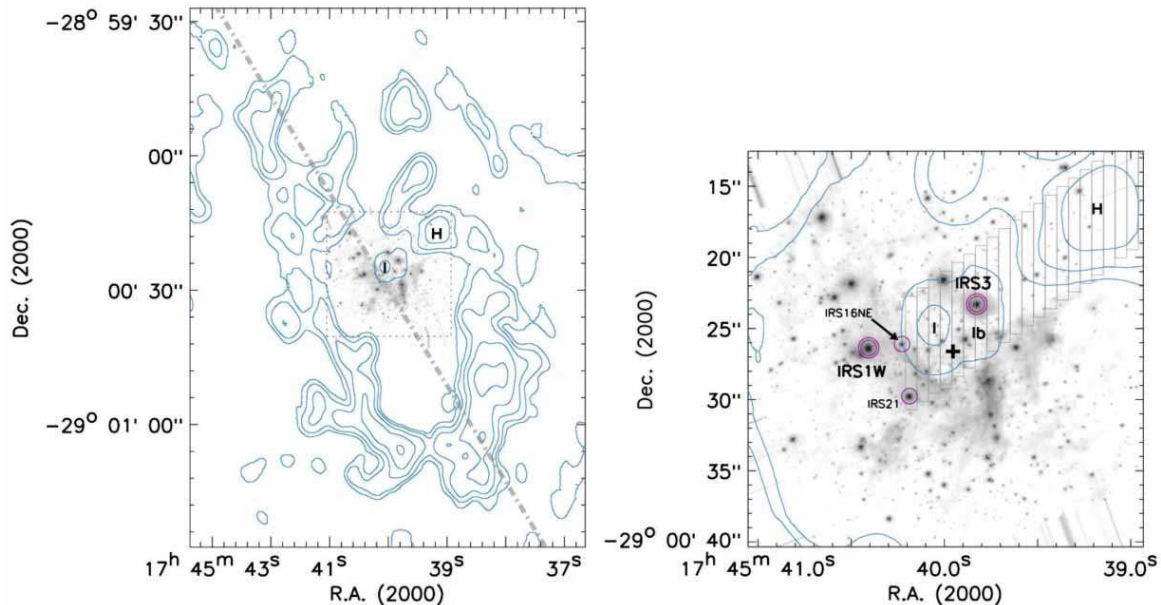


FIG. 1.— *K*-band image of the Central Cluster obtained from ESO NACO archive data with contours of HCN $J=4-3$ emission (Montero-Castaño et al. 2009) from the CND overlaid in blue. Locations of clumps I and H of Montero-Castaño et al. (2009) discussed in Section 4.3.2. are labeled. In the left panel the dot-dashed line is parallel to the Galactic plane and the area shown in the right panel is denoted by a dotted square (originally published in Goto et al. 2013). The locations of the infrared sources are marked with circles in the right panel and extraction apertures of the HCN spectra in Fig. 10 are shown as gray rectangles.

1981; Yusef-Zadeh, Wardle, & Roy 2007). Whatever its cause, the high gas kinetic temperature may help to explain the current low star-forming efficiency in the CMZ (Yusef-Zadeh, Wardle, & Roy 2007; An et al. 2011; Immer et al. 2012) and the top-heavy initial mass function observed in the Central Cluster (Bartko et al. 2010) due to the associated reduction of ambipolar diffusion and increase of the Jeans mass.

Of the previously studied 15 lines of sight within 3 pc of the Galactic plane and longitudinally distributed from the Central Cluster, within 1 pc of the central black hole, Sgr A*, to the Quintuplet Cluster 30 pc east of Sgr A* ($l \sim 0.18^\circ$) (Goto et al. 2008, Oka et al. unpublished), the one toward GCIRS 3, located only a few arcseconds from Sgr A* (Fig. 1), is exceptional. While all 15 sightlines show prominent absorption by H_3^+ in its $R(1,1)^l$ and $R(3,3)^l$ lines, indicating high H_3^+ populations both in the lowest (J, K) = (1,1) level and the (3,3) metastable level 361 K above ground, the $R(2,2)^l$ line is prominent only on the sightline toward GCIRS 3, over a velocity range centered near $+50 \text{ km s}^{-1}$ (Goto et al. 2008). Since the (2,2) level spontaneously decays to ground (1,1) (Pan & Oka 1986) with a lifetime of 27 days (Neale et al. 1996), the density in the gas producing this absorption must be considerably higher than in other regions of the CMZ observed to date. This gas is likely to be in the form of a compact cloud, since the sightline toward GCIRS 1W, which is only $8''.4$ away from GCIRS 3 (0.33 pc, assuming equal radial distances of 8 kpc; Eisenhauer et al. 2003; Ghez et al. 2008), produces a much weaker $R(2,2)^l$ absorption line.

In this paper we present, analyze, and discuss new and improved spectra of H_3^+ toward GCIRS 3 and GCIRS 1W, as well as CO ro-vibrational transition spectra toward them and few other objects in the Central Cluster and the Quintuplet Cluster. The velocity

resolution of the CO spectra is higher by factors of ~ 5 to ~ 100 than previous studies of the CO fundamental band lines toward these objects (Geballe, Baas, & Wade 1989; Moneti, Cernicharo, & Pardo 2001; Moutaka et al. 2009). The ratio of the column densities $N(\text{CO})/N(H_3^+)$ is invariably much lower in diffuse clouds ($n < 300 \text{ cm}^{-3}$) than dense clouds. Thus, observations of both species help to discriminate between dense and diffuse environments.

2. OBSERVATIONS

The observations consisted of high resolution infrared spectroscopy of several Galactic center sources using spectrographs at the Very Large Telescope (VLT) at Paranal in Chile and the Subaru Telescope on Mauna Kea in Hawai'i. A summary of the observations is given in Table 1.

2.1. CRIRES/VLT

Spectra of H_3^+ lines toward GCIRS 3 and GCIRS 1W were obtained using CRIRES (Käufel et al. 2004) at the VLT on several occasions in June and August 2007 in an open time program (079.C-0874). The CRIRES $0''.2$ wide slit, oriented at position angle 113° so that GCIRS 3 and GCIRS 1W could be observed simultaneously, provided a velocity resolution of 3 km s^{-1} . The adaptive optics system MACAO (Bonnet et al. 2004) was used with a $R = 13.5$ mag star $17''$ distant from GCIRS 1W as the wavefront reference. The $R(1,1)^l$ ($3.71548 \mu\text{m}$), $R(2,2)^l$ ($3.62047 \mu\text{m}$), and $R(3,3)^l$ ($3.53366 \mu\text{m}$) lines were observed separately using three grating settings.

Spectra of CO toward GCIRS 3, GCIRS 1W, GCIRS16 NE, GCIRS 21 (all members of the Central Cluster; Fig. 1), and the Quintuplet Cluster source GCS 3-2 were obtained between October 2006 and September 2007 in service observing mode during sci-

TABLE 1
SUMMARY OF OBSERVATIONS.

Object	UT Date	Instrument/Telescope	Lines	Grating ^a	Spec. Res.	Exp. ^b	Standard
GCIRS 3/GCIRS 1W	11 Oct 2006	CRILES/VLT	$^{13}\text{CO } v=1-0$	12/1/n	$R=50,000$	1	HR 6879
GCIRS 3/GCIRS 1W	11 Oct 2006	CRILES/VLT	$^{13}\text{CO } v=1-0$	12/1/i	$R=50,000$	1	HR 6879
GCIRS 3/GCIRS 1W	9 Jun, 4-5 Aug 2007	CRILES/VLT	$H_3^+ R(1,1)^l$	3739.4	$R=100,000$	108	HR 6879
GCIRS 3/GCIRS 1W	5, 9, 10 Aug 2007	CRILES/VLT	$H_3^+ R(2,2)^l$	3646.1	$R=100,000$	126	HR 6879
GCIRS 3/GCIRS 1W	10, 28 Aug 2007	CRILES/VLT	$H_3^+ R(3,3)^l$	3533.6	$R=100,000$	108	HR 6879
GCIRS 16NE/GCIRS 21	13 May 2007	CRILES/VLT	$^{12}\text{CO } v=2-0$	2239.2	$R=100,000$	40	HR 6879
GCIRS 16NE/GCIRS 21	14 May 2007	CRILES/VLT	$^{12}\text{CO } v=2-0$	2336.2	$R=100,000$	40	HR 6879
GCS 3-2	15 Sep 2007	CRILES/VLT	$^{12}\text{CO } v=2-0$	2239.2	$R=100,000$	16	HR 6879
GCS 3-2	15 Sep 2007	CRILES/VLT	$^{12}\text{CO } v=2-0$	2336.2	$R=100,000$	16	HR 6879
GCS 3-2	27 Jul 2008	CRILES/VLT	$H_2 v=1-0 S(0)$	2236.1	$R=100,000$	80	HR 6879
GCS 3-2	15 Oct 2007	CRILES/VLT	$H_2 v=1-0 S(1)$	2117.6	$R=100,000$	40	HR 6879
GCS 3-2	17 Aug 2008	CRILES/VLT	$H_2 v=1-0 S(1)$	2117.6	$R=100,000$	40	HR 6879
GCS 3-2	24 May 2003	IRCS/SUBARU	$H_2 v=1-0 S(0)$	4300/200	$R=20,000$	60	HR 7557, HR 7194

^a For CRILES these are reference wavelength in nm, or grating setting name for 2006 observations only. For IRCS the entry is echelle and cross-disperser angle.

^b Total integration time in minutes.

ence verification time for CRILES (60.A-9057) as well as in the open time program (079.C-0874), using the same adaptive optics set-up as described above and an $R = 15$ mag star $8''$ away from GCS 3-2 as a wavefront reference for that object. The $^{12}\text{CO } v=2-0$ overtone band, which has been used by us previously (Oka et al. 2005) was observed for GCIRS16 NE, GCIRS 21, and GCS 3-2, but not for GCIRS 3 and GCIRS 1W, since those objects are faint in the K -band; for them the fundamental band $v=1-0$ was observed. For the overtone band, the spectral range 2.292–2.356 μm was covered in two grating settings, allowing measurements of all R -branch lines and the $P(1)$ – $P(4)$ lines. For the fundamental band, the spectral range 4.692–4.809 μm was observed in two grating settings covering the $P(3)$ to $P(15)$ lines of $^{12}\text{CO } v=1-0$ and the $R(9)$ – $R(0)$ and $P(1)$ – $P(4)$ lines of $^{13}\text{CO } v=1-0$. The $^{12}\text{CO } v=1-0$ lines are heavily saturated and have not been analyzed, unless otherwise noted. The $0''.4$ slit was used for GCIRS 3 and GCIRS 1W while the $0''.2$ slit was used for the other objects, resulting in velocity resolutions of 6 km s^{-1} and 3 km s^{-1} , respectively. The early-type star HR 6879 (B 9.5III, $R=1.85$ mag) was observed before or after each GC object as a telluric standard.

Spectra of GCS 3-2 were also obtained by CRILES in the intervals 2.200–2.255 μm and 2.087–2.133 μm to search for absorption from two quadruple transitions of H_2 , $v=1-0 S(0)$ and $v=1-0 S(1)$, in the same open time program. The $0''.2$ slit was employed, resulting in a velocity resolution of 3 km s^{-1} .

Spectra were extracted from the CRILES data using the `crires_spec_jitter` recipe⁹ on the ESO gasgano platform¹⁰. The results were consistent with the pre-processed CRILES spectra provided by the observatory. In some cases the latter spectra were cosmetically better and were used for analysis. Custom-written IDL code was employed to divide spectra of the GC sources by the spectra of the telluric standard to remove atmospheric absorption lines. Wavelength calibration was obtained by cross-correlating the telluric absorption lines with

model atmospheric transmission spectra computed using ATRAN (Lord 1992). The uncertainty in the wavelength calibration depends on the density of telluric lines and is typically less than one pixel ($\leq 1 \text{ km s}^{-1}$). The IRAF¹¹ *rv* package was used to convert the observed wavelengths to velocity with respect to the local standard of the rest utilizing the IAU definition of the Sun's peculiar motion.

2.2. IRCS/Subaru

The spectrograph IRCS at the Subaru Telescope was used to obtain a spectrum of GCS 3-2 in the vicinity of the $H_2 v=1-0 S(0)$ line on 24 May 2003 UT. The slit width was $0''.15$, resulting in a velocity resolution of 15 km s^{-1} . The adaptive optics system was used employing the same wavefront reference as for the CRILES observations of GCS 3-2. The slit was oriented east-west. HR 7557 ($R=0.77$ mag, A7 V) and HR 7121 ($R=2.02$ mag, B2.5 V) were observed as telluric standard stars. Reduction of the IRCS data was performed in the similar manner as for the CRILES data except that the IRAF aperture extraction package was used to extract the spectra.

3. RESULTS

3.1. H_3^+

The spectra of the three H_3^+ lines toward GCIRS 3 and GCIRS 1W are shown in Fig. 2 together with the spectrum of the $v=1-0 P(1)$ line of ^{13}CO . The $P(1)$ line was selected for comparison because it is least affected by nearby telluric absorption lines and interstellar ^{12}CO lines, as discussed in Section 3.2. The systemic radial velocity of GCIRS 1W is $+35 \pm 20 \text{ km s}^{-1}$ (Paumard et al. 2006), measured by He I absorption line at 2.06 μm (Paumard et al. 2004). The radial velocity of GCIRS 3 is not known due to the absence of photospheric lines in its spectrum.

3.1.1. Negative velocities

¹¹ IRAF is distributed by the National Optical Astronomy Observatories, which are operated by the Association of Universities for Research in Astronomy, Inc., under cooperative agreement with the National Science Foundation.

⁹ CRILES Pipeline User Manual VLT-MAN-ESO-19500-4406.

¹⁰ <http://www.eso.org/sci/data-processing/software/gasgano/>.

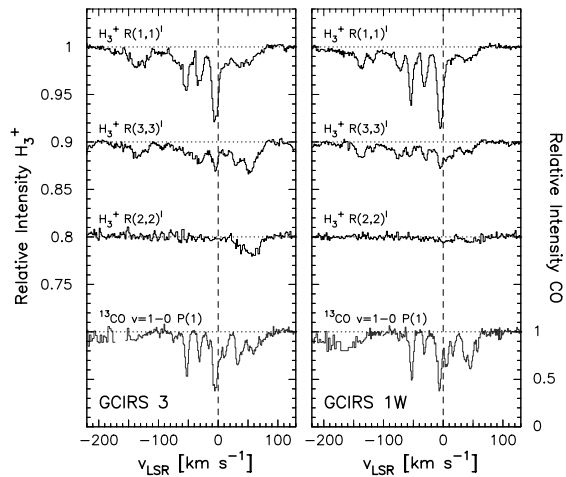


FIG. 2.— Velocity profiles of H_3^+ $R(1,1)^l$, $R(3,3)^l$, $R(2,2)^l$, and ^{13}CO $v=1-0$ $P(1)$ lines toward GCIRS 3 (left) and GCIRS 1W (right).

At negative velocities the spectra in Fig. 2 are similar to those on the sightlines toward GCS 3-2 (Oka et al. 2005, located in the Quintuplet Cluster) and NHS 21, NHS 22, NHS 25, and NHS 42 (Goto et al. 2008, located between the Quintuplet and the Central Clusters). Our interpretation of them is similar to those authors. The three sharp absorption components at -53 km s^{-1} , -32 km s^{-1} , and 0 km s^{-1} , conspicuous in both the H_3^+ $R(1,1)^l$ and ^{13}CO $P(1)$ profiles, are due to relatively cold and dense gas in the lateral arms at 3 kpc and 4 kpc approaching the sun, and to foreground spiral arms, respectively. The same sets of the absorption lines have been observed in CO $J=3-2$ (Sutton et al. 1990; Moneti, Cernicharo, & Pardo 2001) and NH_3 (Serabyn & Güsten 1986) toward the Galactic center. In common with the previously observed sightlines from the Central Cluster to 30 pc east, absorption by CO 2–0 band lines at negative velocities is almost entirely due to gas in these arms. In contrast, at negative velocities the H_3^+ $R(1,1)^l$ spectrum shows a broad and structured absorption trough upon which the three sharp absorptions due to the arms are superimposed. No absorption in the $R(2,2)^l$ line is present, indicating that the density of the gas producing the absorption troughs in the $R(1,1)^l$ and $R(3,3)^l$ line profiles is low. We therefore identify the absorption trough with diffuse gas in the CMZ, as in Oka et al. (2005).

It is noteworthy that at negative velocities the $R(3,3)^l$ absorption profile, which contains no spiral arm components, matches the shape of the $R(1,1)^l$ trough. This similarity is clearly seen in Fig. 3 in which the spectra of the $R(3,3)^l$ line, multiplied by a factor of 1.3 for each object, are superimposed on the spectra of the $R(1,1)^l$ line. This likeness has been noted earlier (Oka et al. 2005; Goto et al. 2008), but has not previously been seen in such detail as in Fig. 3. It provides conclusive evidence that the trough in the $R(1,1)^l$ spectrum and the $R(3,3)^l$ spectrum arise in the same warm and diffuse gas. Indeed the accurate match indicates remarkably that although the gas that produces the absorption trough covers a wide range of velocities and presumably thus exists over a wide range of line of sight locations within the CMZ,

its temperature is nearly constant.

At negative velocities the $R(3,3)^l$ profiles, and in particular the one toward GCIRS 1W, also contain several weak and narrow absorption features. Some of these are close to the velocities of the foreground arms and might be interpreted as indicating the presence of warm gas in the spiral arms. We do not adopt this interpretation in view of the absence of such features in the $R(3,3)^l$ spectra on other sightlines and because close examination reveals that the velocities of the absorption peaks are not exact matches to those of the spiral arms (as observed in the CO $P(1)$ and H_3^+ $R(1,1)^l$ line profiles). It may be that they arise in compact and warm regions of the Circumnuclear Disk (CND; Genzel & Townes 1987), the chain of molecular clouds orbiting Sgr A* at $v \sim 100 \text{ km s}^{-1}$ at a radius of 1.5 pc (Zhao et al. 2009).

3.1.2. Positive velocities

At positive velocities the absorption profiles of the H_3^+ lines toward GCIRS 3 and GCIRS 1W are qualitatively different in two ways from those toward the other GC sources outside the Central Cluster shown in Oka et al. (2005) and Goto et al. (2008). First, absorption toward other GC stars is only present to about $+30 \text{ km s}^{-1}$, whereas absorption extends to $+60 \text{ km s}^{-1}$ toward GCIRS 1W and to $+80 \text{ km s}^{-1}$ toward GCIRS 3, in both the $R(1,1)^l$ and the $R(3,3)^l$ lines (Fig. 2). Note that these velocity extents are also present in the ^{13}CO line in this figure. Second, the sightline toward GCIRS 3 also produces strong and broad absorption at positive velocities in the $R(2,2)^l$ line (from $+20$ to $+70 \text{ km s}^{-1}$, peaking at $+52 \text{ km s}^{-1}$). The only other sightline for which this line has been seen strongly is that toward 2MASS J17470898-2829561, which is apparently located within the Sgr B molecular cloud (Geballe & Oka 2010; Goto et al. 2011), far removed from the central few parsecs. The $R(3,3)^l$ profile toward GCIRS 3 has two absorption maxima, at $+28 \text{ km s}^{-1}$ and $+52 \text{ km s}^{-1}$, whereas the $R(2,2)^l$ profile has only a single maximum near $+52 \text{ km s}^{-1}$.

Only a marginal detection of the $R(2,2)^l$ absorption near $+40 \text{ km s}^{-1}$ is evident toward GCIRS 1W (Fig. 2, right). Assuming that both GCIRS 1W and GCIRS 3 are members of the Central Cluster (see discussion below), the large differences in the H_3^+ and ^{13}CO line profiles at positive velocities, on sightlines separated by 0.33 pc, suggests that the cloud (or clouds) producing the $R(2,2)^l$ absorption toward GCIRS 3 is compact, with linear dimension comparable to the sightline separation, and is located close to the Central Cluster.

3.1.3. Equivalent widths and column densities

As noted previously, apart from velocities near those of the spiral arms ($-62 \rightarrow -45 \text{ km s}^{-1}$, $-37 \rightarrow -25 \text{ km s}^{-1}$, and $-15 \rightarrow +12 \text{ km s}^{-1}$) and at positive velocities for GCIRS 3, a nearly constant scaling factor of 1.3 exists between the $R(3,3)^l$ and $R(1,1)^l$ absorption profiles, as shown in Fig. 3. To estimate the strengths of the $R(1,1)^l$ absorptions originating in the CMZ in the above velocity intervals, and thus to estimate the total column densities of H_3^+ in the CMZ, we assume the same factor also applies in the above velocity intervals, multiply the $R(3,3)^l$

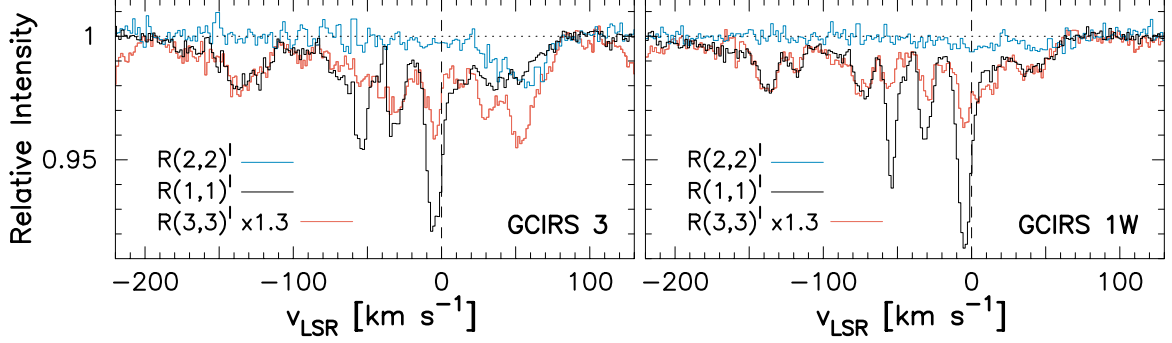


FIG. 3.— Left: Absorption velocity profiles of H_3^+ $R(1,1)^l$ (black), $R(3,3)^l$ (red), and $R(2,2)^l$ (blue) toward GCIRS 3. $R(3,3)^l$ absorption is scaled by the factor of 1.3 to match the broad absorption trough of the $R(1,1)^l$ line. Right: Same, but for GCIRS 1W.

line profiles by 1.3, and use them as surrogates for the $R(1,1)^l$ CMZ absorptions toward these objects. This appears to be a more accurate method than the one used by Oka et al. (2005), which did not include the velocity structure in the trough that is now evident in the $R(3,3)^l$ absorption profile observed by CRIRES.

The equivalent widths of those portions of the H_3^+ lines arising in the CMZ, together with the corresponding column densities of the lower levels of the transitions, are listed in Table 2 over several sub-intervals covering the entire CMZ velocity range. The column densities were calculated using $N(\text{H}_3^+)_{\text{level}} = (3hc/8\pi^3\lambda)W_\lambda/|\mu|^2$, where $|\mu|^2$, the square of the dipole moment, is 0.0141 D², 0.0177 D², and 0.0191 D² for the $R(1,1)^l$, $R(2,2)^l$, and $R(3,3)^l$ transitions, respectively. The Einstein A coefficients, given in Neale et al. (1996), were also used in our previous studies (Goto et al. 2002; Oka et al. 2005; Goto et al. 2008). Uncertainties in the equivalent widths were estimated from the standard deviations in the nearby continuum multiplied by the wavelength interval. To determine the H_3^+ absorption equivalent width and associated column density due to gas in the spiral arms toward each source, we subtracted the scaled $R(3,3)^l$ surrogates from the $R(1,1)^l$ absorption profiles. The resulting values are given in Table 3.

3.2. CO

Velocity profiles of lines of the ^{13}CO $v=1-0$ fundamental band toward GCIRS 3, GCIRS 1W and of lines of the ^{12}CO $v=2-0$ overtone band toward GCIRS 16NE, GCIRS 21, GCS 3-2 are shown in Figs. 4 and 5. In Fig. 6 for each of these sources a profile of the $R(0)$ line from either the 1-0 band of ^{13}CO or from the 2-0 band of ^{12}CO is shown. In Figs. 4 and 5 there are numerous gaps in the profiles due to strong telluric absorption lines. In addition some of the ^{13}CO line profiles overlap with those of strong lines of the ^{12}CO fundamental. The ^{13}CO $v=1-0$ $R(J)$ lines nearly coincide with the C^{18}O $v=1-0$ $R(J+1)$ lines, with velocity offsets of 50–95 km s⁻¹. The ^{13}CO $v=1-0$ $P(J)$ lines nearly coincide with C^{18}O $v=1-0$ $P(J-1)$ lines with offsets of 18–30 km s⁻¹. However in each case the contamination is relatively minor. C^{18}O $v=1-0$ $R(0)$ is the only observed transition that is not contaminated by lines of ^{12}CO and ^{13}CO ; a simple comparison of the line depths of C^{18}O $R(0)$ and ^{13}CO $R(0)$ (the former shown at the bottom of Fig. 4) indicates that C^{18}O abundance is less than 1/4 of that of ^{13}CO . The ra-

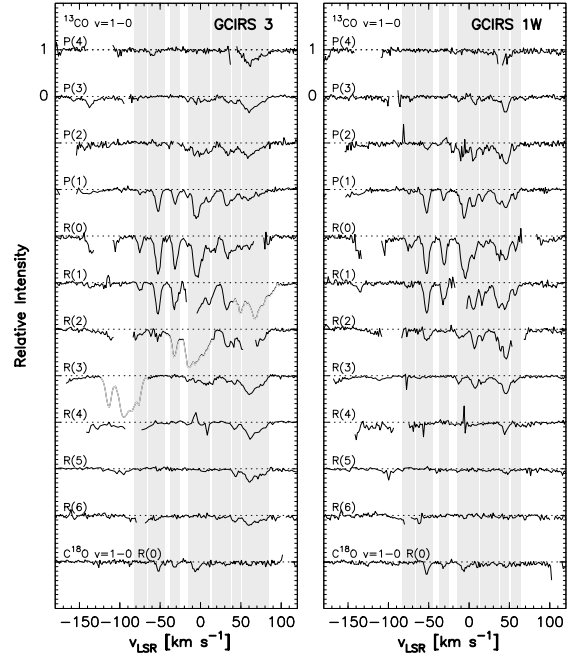


FIG. 4.— Velocity profiles of ^{13}CO $v=1-0$ $P(4)-P(1)$, $R(0)-R(6)$ and ^{18}CO $v=1-0$ $R(0)$ absorption lines toward GCIRS 3 (left) and GCIRS 1W (right). Portions of the profiles contaminated by ^{12}CO $v=1-0$ are shown as gray lines. Velocity intervals used in the analysis are denoted by shaded vertical strips.

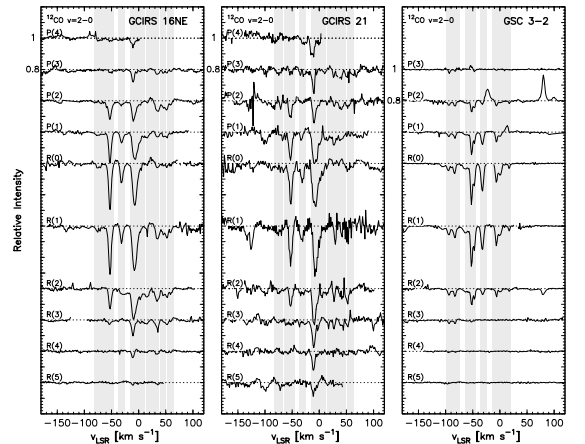


FIG. 5.— Spectra of ^{12}CO $v=2-0$ $P(3)-P(1)$ and $R(0)-R(5)$ lines on sightlines to GCIRS 16NE, GCIRS 21, and GCS 3-2. Individual velocity components are shaded.

TABLE 2
EQUIVALENT WIDTHS W_λ AND COLUMN DENSITIES OF H_3^+ IN THE CMZ TOWARD GCIRS 3 AND GCIRS 1W.

Object	v_{LSR} [km s $^{-1}$]	W_λ [$10^{-6}\mu\text{m}$]			$N(J, K)$ [10^{14}cm^{-2}]		
		$R(1,1)^l$	$R(3,3)^l$	$R(2,2)^l$	(1,1)	(3,3)	(2,2)
GCIRS 3	$-180 \rightarrow -109$	9.43 ± 1.59	7.49 ± 1.10	< 2.51	4.33 ± 0.73	2.66 ± 0.39	< 0.94
	$-109 \rightarrow +1^a$	21.3 ± 2.5	16.4 ± 1.7	< 4.17	9.75 ± 1.17	5.82 ± 0.61	< 1.56
	$+1 \rightarrow +38^b$	2.15 ± 1.06	1.48 ± 1.01	< 1.14	0.99 ± 0.49	0.53 ± 0.36	< 0.43
	$+38 \rightarrow +51^b$	0.66 ± 0.34	2.02 ± 0.36	1.14 ± 0.40	0.30 ± 0.16	0.72 ± 0.13	0.43 ± 0.15
	$+51 \rightarrow +85^b$	2.30 ± 0.98	5.51 ± 0.93	3.98 ± 1.10	1.05 ± 0.45	1.96 ± 0.33	1.49 ± 0.41
GCIRS 1W	$-180 \rightarrow -109$	8.91 ± 1.22	6.00 ± 0.96	< 1.67	4.09 ± 0.56	2.13 ± 0.34	< 0.63
	$-109 \rightarrow +1^a$	19.2 ± 1.9	14.8 ± 1.5	< 2.62	8.82 ± 0.88	5.26 ± 0.53	< 0.98
	$+1 \rightarrow +38$	6.58 ± 0.65	5.49 ± 0.50	1.04 ± 0.81	3.02 ± 0.30	1.95 ± 0.18	0.39 ± 0.31
	$+38 \rightarrow +51$	1.71 ± 0.20	1.36 ± 0.15	0.76 ± 0.28	0.79 ± 0.09	0.48 ± 0.05	0.28 ± 0.11
	$+51 \rightarrow +64$	0.74 ± 0.19	0.46 ± 0.15	0.40 ± 0.24	0.34 ± 0.09	0.16 ± 0.05	0.15 ± 0.09

^a Equivalent widths of $R(1,1)^l$ at the velocity range $-109 \rightarrow +1$ km s $^{-1}$ are calculated by scaling $R(3,3)^l$ absorption lines at the same velocity interval by the factor of 1.3 so that $R(3,3)^l$ matches to the trough absorption of $R(1,1)^l$, in order to disentangle the absorptions in the CMZ from the foreground arm clouds.

^b Equivalent widths of $R(1,1)^l$, $R(3,3)^l$, and $R(2,2)^l$ toward GCIRS 1W are subtracted to isolate the local absorption components of H_3^+ to GCIRS 3.

tio above should be taken as an upper limit, since ^{13}CO $R(0)$ is expected to be more saturated than C^{18}O $R(0)$.

The measured equivalent widths and calculated column densities of the least contaminated ^{13}CO $v=1-0$ and ^{12}CO $v=2-0$ lines are listed in Tables 4 and 6. For the H_3^+ and ^{12}CO $v=2-0$ lines, the absorption strengths ΔI and optical depths τ are approximately proportional, because the maximum optical depths are 0.1–0.3. For the fundamental band of ^{13}CO , however, the non-linear equations $\Delta I(\lambda) = I_0(1 - e^{-\tau(\lambda)})$ and $W_\lambda = \int \tau(\lambda) d\lambda$ must be used to relate the two, because the peak absorptions are as large as 80%. The column densities of CO were calculated using the same equation as for H_3^+ , but with $|\mu|^2 = \frac{S}{2J+1}(\mu_{1-0/2-0})^2$, where the spectral strength S is $J+1$ for $R(J)$ lines and J for $P(J)$ lines and $\mu_{1-0}=0.1055$ D, $\mu_{2-0}=6.53 \times 10^{-3}$ D are the dipole moments of ^{12}CO $v=1-0$ and $v=2-0$ transitions, respectively (Zou & Varanasi 2002). The small differences between the transition dipole moments of ^{12}CO $v=1-0$ and ^{13}CO $v=1-0$ lines (Chackerian & Tipping 1983) were neglected. Population diagrams, from which temperatures can be estimated, are shown in Fig. 7 in velocity intervals corresponding to the various cloud and gas environments.

At negative velocities the dominant CO absorbers on all sightlines to the Central Cluster are the spiral and lateral arms. An additional and weaker absorption at -72 km s $^{-1}$ is present toward GCIRS 1, GCIRS 3, and GCIRS 16NE. In all of these the highest rotational level observed at negative velocities is $J=3$, and excitation temperatures range from 7 to 19 K (Table ??, and also Fig. 7), depending on the line of sight and the line pair. It is likely that the population distribution is subthermal (Neufeld 2012). The total column densities of ^{13}CO in the three foreground arms were determined by summing the level populations using the values in Table 5 and are about 8×10^{16} cm $^{-2}$ toward each source. This is in reasonable agreement with the value of 1.1×10^{17} cm $^{-2}$ of Moneti, Cernicharo, & Pardo (2001) based on lower resolution ($R=2000$) spectroscopy of ^{13}CO $v=1-0$ over an extended region near Sgr A*.

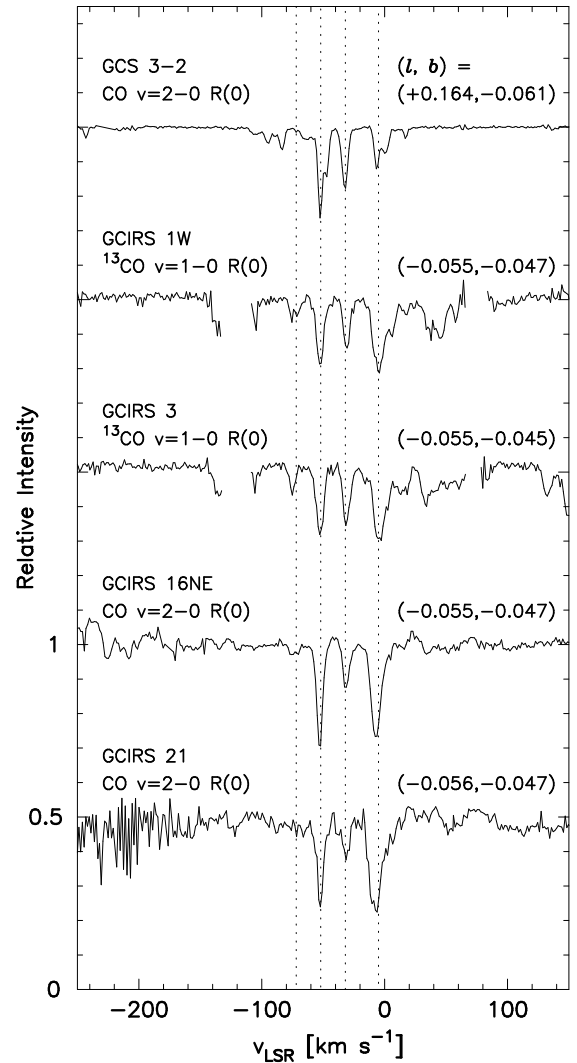


FIG. 6.— Velocity profiles of CO $R(0)$ lines for five Galactic center sources (Galactic coordinates indicated on the right). Dashed lines from left to right correspond to radial velocities of an unidentified contributor at -72 km s $^{-1}$, the 3 kpc expanding arm, the 4 kpc expanding arm, and clouds in more local arms as well as other clouds in circular orbits.

TABLE 3

EQUIVALENT WIDTHS W_λ AND COLUMN DENSITIES OF H_3^+ IN THE GALACTIC ARM CLOUDS TOWARD GCIRS 3 AND TOWARD GCIRS 1W.

Object	v_{LSR} [km s $^{-1}$]	W_λ ^a [10 $^{-6}$ μm] $R(1,1)^l$	$N(J, K)^a$ [10 14 cm $^{-2}$] (1,1)
GCIRS 3	−62 → −45	2.95±0.72	1.35±0.33
	−37 → −25	0.78±0.51	0.36±0.23
	−15 → +12	6.57±1.17	3.01±0.54
GCIRS 1W	−62 → −45	3.61±0.57	1.66±0.26
	−37 → −25	1.88±0.39	0.86±0.18
	−15 → +12	5.90±0.94	2.71±0.43

^a After removal of CMZ trough component, assumed to be given by the $R(3,3)^l$ absorption profile scaled by 1.3.TABLE 4
EQUIVALENT WIDTHS W_λ OF CO.

	v_{LSR} [km s $^{-1}$] $^{13}\text{CO } v=1-0$	$P(4)$	$P(3)$	$P(2)$	$P(1)$	$R(0)$	W_λ [10 $^{-5}$ μm] $R(1)$	$R(2)$	$R(3)$	$R(4)$	$R(5)$	$R(6)$
GCIRS 3	−82 → −65	—	—	—	0.86	2.86	1.18	2.24	—	—	—	—
	−65 → −45	—	—	—	6.13	15.07	9.94	2.45	—	—	—	—
	−37 → −25	—	—	—	3.20	10.39	8.28	—	—	—	—	—
	−15 → +12	—	2.08	8.61	18.08	33.04	—	—	4.41	—	—	—
	+12 → +38	—	—	5.08	7.06	11.33	14.33	7.48	2.61	—	—	—
	+38 → +51	—	1.54	3.11	3.39	5.64	—	6.05	2.54	1.86	1.72	1.66
	+51 → +85	11.05	10.28	9.60	6.93	—	—	—	14.19	11.43	8.34	6.52
	v_{LSR} [km s $^{-1}$] $^{13}\text{CO } v=1-0$	$P(4)$	$P(3)$	$P(2)$	$P(1)$	$R(0)$	W_λ [10 $^{-5}$ μm] $R(1)$	$R(2)$	$R(3)$	$R(4)$	$R(5)$	$R(6)$
GCIRS 1W	−82 → −65	—	—	—	—	—	—	—	—	—	—	—
	−65 → −45	—	—	—	6.67	14.81	9.82	3.54	—	—	—	—
	−37 → −25	—	—	—	2.01	8.43	5.27	—	—	—	—	—
	−15 → +12	—	1.99	9.09	16.74	33.13	—	8.02	4.57	—	—	—
	+12 → +38	3.33	1.91	5.36	6.13	7.83	12.79	5.04	3.29	—	—	—
	+38 → +51	—	5.08	8.67	7.59	9.92	12.53	14.06	6.48	2.65	1.11	—
	+51 → +64	—	—	1.48	2.36	2.63	3.34	—	1.70	0.56	—	—
	v_{LSR} [km s $^{-1}$] $^{12}\text{CO } v=2-0$	$P(4)$	$P(3)$	$P(2)$	$P(1)$	$R(0)$	W_λ [10 $^{-6}$ μm] $R(1)$	$R(2)$	$R(3)$	$R(4)$	$R(5)$	
GCIRS 16NE	−82 → −65	—	—	1.34	2.15	2.11	2.75	—	—	—	—	—
	−65 → −45	1.56	1.46	8.30	10.53	16.20	16.99	6.03	1.73	—	—	—
	−37 → −25	0.89	—	1.94	3.81	6.41	4.83	2.75	—	—	—	—
	−15 → +12	3.45	5.10	10.53	19.48	23.97	25.96	21.01	6.62	1.66	1.06	—
	+12 → +38	—	1.90	3.68	3.59	—	4.57	8.43	4.51	1.00	—	—
	+38 → +51	—	1.52	4.17	2.03	1.04	4.63	3.41	—	—	—	—
	+51 → +64	—	1.00	2.75	1.47	0.94	4.03	3.21	—	—	—	—
	v_{LSR} [km s $^{-1}$] $^{12}\text{CO } v=2-0$	$P(4)$	$P(3)$	$P(2)$	$P(1)$	$R(0)$	W_λ [10 $^{-6}$ μm] $R(1)$	$R(2)$	$R(3)$	$R(4)$	$R(5)$	
GCIRS 21	−82 → −65	—	—	—	—	—	—	—	—	—	—	—
	−65 → −45	—	—	6.45	11.17	16.93	11.73	5.49	—	—	—	—
	−37 → −25	2.13	2.31	—	—	6.76	5.51	2.52	—	—	—	—
	−15 → +12	7.76	7.83	8.96	22.44	32.61	28.06	19.72	11.37	7.38	—	—
	+12 → +38	—	—	—	—	—	—	—	—	—	—	—
	+38 → +51	—	—	3.39	3.29	—	—	3.71	2.87	—	—	—
	+51 → +64	—	—	—	—	2.73	—	3.53	—	—	—	—
	v_{LSR} [km s $^{-1}$] $^{12}\text{CO } v=2-0$	$P(3)$	$P(2)$	$P(1)$	$R(0)$	W_λ [10 $^{-6}$ μm] $R(1)$	$R(2)$	$R(3)$	$R(4)$	$R(5)$		
GCS 3-2	−98 → −75	0.84	3.15	3.06	5.50	6.96	4.25	1.70	0.50	—	—	—
	−75 → −65	—	—	—	1.29	1.41	0.49	—	—	—	—	—
	−65 → −45	—	4.77	8.30	16.73	17.29	6.97	0.99	—	—	—	—
	−37 → −25	—	—	3.55	8.65	6.98	1.70	—	—	—	—	—
	−15 → +12	—	1.69	2.81	9.18	7.66	2.74	—	—	—	—	—
	+12 → +21	—	0.54	—	1.04	0.87	0.55	—	—	—	—	—

At positive velocities, as in the case of H_3^+ it seems likely that most or all of the absorption by CO arises within the CMZ. At $0 < v < +38$ km s $^{-1}$ absorption toward GCIRS 1W, GCIRS 3, and GCIRS 16NE is observed only up to $J=3$. At higher positive velocities, a weak and narrow +45 km s $^{-1}$ absorption is observed toward GCIRS 1W out to $J=5$, and a similar +43 km s $^{-1}$

absorption is observed toward GCIRS 3 out to $J=6$. Most strikingly, a strong and broad absorption centered near +60 km s $^{-1}$ is present toward GCIRS 3 also up to $J=6$ for ^{13}CO , and up to $J=15$ for ^{12}CO , but is not observed toward GCIRS 1W. The velocity range of this feature is similar to those of the positive velocity features seen toward GCIRS 3 in H_3^+ lines, indicating that the absorptions by each species probably originate in physically

TABLE 5
LEVEL COLUMN DENSITIES OF CO.

	$v_{\text{LSR}} [\text{km s}^{-1}]$ $^{13}\text{CO } v=1-0$	$P(4)$	$P(3)$	$P(2)$	$P(1)$	$N_{\text{CO}} [10^{15} \text{cm}^{-2}]$						
						$R(0)$	$R(1)$	$R(2)$	$R(3)$	$R(4)$	$R(5)$	$R(6)$
GCIRS 3	− 82→− 65	—	—	—	1.17	1.29	0.80	1.70	—	—	—	—
	− 65→− 45	—	—	—	8.30	6.83	6.77	1.86	—	—	—	—
	− 37→− 25	—	—	—	4.34	4.71	5.64	—	—	—	—	—
	− 15→+ 12	—	2.19	9.71	24.50	14.97	—	—	3.52	—	—	—
	+ 12→+ 38	—	—	5.72	9.57	5.13	9.76	5.67	2.08	—	—	—
	+ 38→+ 51	—	1.62	3.51	4.59	2.56	—	4.58	2.03	1.52	1.44	1.41
	+ 51→+ 85	11.17	10.80	10.82	9.38	—	—	—	11.31	9.39	6.99	5.55
	$v_{\text{LSR}} [\text{km s}^{-1}]$ $^{13}\text{CO } v=1-0$	$P(4)$	$P(3)$	$P(2)$	$P(1)$	$N_{\text{CO}} [10^{15} \text{cm}^{-2}]$						
						$R(0)$	$R(1)$	$R(2)$	$R(3)$	$R(4)$	$R(5)$	$R(6)$
GCIRS 1W	− 82→− 65	—	—	—	—	—	—	—	—	—	—	—
	− 65→− 45	—	—	—	9.03	6.71	6.69	2.69	—	—	—	—
	− 37→− 25	—	—	—	2.72	3.82	3.59	—	—	—	—	—
	− 15→+ 12	—	2.09	10.25	22.69	15.01	—	6.08	3.64	—	—	—
	+ 12→+ 38	3.36	2.01	6.04	8.31	3.55	8.71	3.82	2.62	—	—	—
	+ 38→+ 51	—	5.34	9.78	10.29	4.50	8.53	10.66	5.17	2.18	0.93	—
	+ 51→+ 64	—	—	1.67	3.20	1.19	2.28	—	1.35	0.46	—	—
	$v_{\text{LSR}} [\text{km s}^{-1}]$ $^{12}\text{CO } v=2-0$	$P(4)$	$P(3)$	$P(2)$	$P(1)$	$N_{\text{CO}} [10^{17} \text{cm}^{-2}]$						
						$R(0)$	$R(1)$	$R(2)$	$R(3)$	$R(4)$	$R(5)$	
GCIRS 16NE	− 82→− 65	—	—	0.81	1.55	0.51	0.99	—	—	—	—	—
	− 65→− 45	0.84	0.82	4.97	7.58	3.89	6.13	2.42	0.73	—	—	—
	− 37→− 25	0.48	—	1.16	2.74	1.54	1.74	1.10	—	—	—	—
	− 15→+ 12	1.86	2.85	6.30	14.02	5.76	9.36	8.43	2.79	0.72	0.47	—
	+ 12→+ 38	—	1.06	2.20	2.58	—	1.65	3.38	1.90	0.43	—	—
	+ 38→+ 51	—	0.85	2.50	1.46	0.25	1.67	1.37	—	—	—	—
	+ 51→+ 64	—	0.56	1.65	1.05	0.23	1.45	1.29	—	—	—	—
	$v_{\text{LSR}} [\text{km s}^{-1}]$ $^{12}\text{CO } v=2-0$	$P(4)$	$P(3)$	$P(2)$	$P(1)$	$N_{\text{CO}} [10^{17} \text{cm}^{-2}]$						
						$R(0)$	$R(1)$	$R(2)$	$R(3)$	$R(4)$	$R(5)$	
GCIRS 21	− 82→− 65	—	—	—	—	—	—	—	—	—	—	—
	− 65→− 45	—	—	3.86	8.04	4.07	4.23	2.20	—	—	—	—
	− 37→− 25	1.15	1.29	—	—	1.62	1.99	1.01	—	—	—	—
	− 15→+ 12	4.17	4.37	5.37	16.15	7.83	10.12	7.91	4.79	3.20	—	—
	+ 12→+ 38	—	—	—	—	—	—	—	—	—	—	—
	+ 38→+ 51	—	—	2.03	2.37	—	—	1.49	1.21	—	—	—
	+ 51→+ 64	—	—	—	—	0.66	—	1.41	—	—	—	—
	$v_{\text{LSR}} [\text{km s}^{-1}]$ $^{12}\text{CO } v=2-0$	$P(4)$	$P(3)$	$P(2)$	$P(1)$	$N_{\text{CO}} [10^{17} \text{cm}^{-2}]$						
						$R(0)$	$R(1)$	$R(2)$	$R(3)$	$R(4)$	$R(5)$	
GCS 3-2	− 98→− 75	—	0.47	1.89	2.20	1.32	2.51	1.70	0.72	0.22	—	—
	− 75→− 65	—	—	—	—	0.31	0.51	0.20	—	—	—	—
	− 65→− 45	—	—	2.86	5.97	4.02	6.23	2.80	0.42	—	—	—
	− 37→− 25	—	—	—	2.55	2.08	2.52	0.68	—	—	—	—
	− 15→+ 12	—	—	1.02	2.02	2.20	2.76	1.10	—	—	—	—
	+ 12→+ 21	—	—	0.32	—	0.25	0.31	0.22	—	—	—	—

TABLE 6
LEVEL COLUMN DENSITIES OF CO.

^{12}CO	3 kpc Arm −65→−45 km s^{-1}		4 kpc Arm −37→−25 km s^{-1}		0 km s^{-1} (Spiral arms + GC) −15→+12 km s^{-1}	
	$N_{\text{CO}} [10^{17} \text{cm}^{-2}]$	$T_{\text{ex}} [\text{K}]$	$N_{\text{CO}} [10^{17} \text{cm}^{-2}]$	$T_{\text{ex}} [\text{K}]$	$N_{\text{CO}} [10^{17} \text{cm}^{-2}]$	$T_{\text{ex}} [\text{K}]$
GCIRS 16NE	16.6± 0.9	11.4± 0.6	6.2± 0.5	12.3± 1.0	30.6± 1.3	14.6± 0.5
GCIRS 21	13.8± 1.7	8.4± 1.3	9.5± 1.7	19.1± 3.2	42.6± 3.4	17.4± 1.2
GCS 3-2	13.6± 0.8	8.4± 0.4	5.4± 0.4	6.1± 0.4	6.2± 0.9	7.2± 0.8
Average	14.7± 0.7	9.4± 0.7	7.0± 0.6	12.5± 3.8	26.5± 1.2	13.1± 0.7

NOTE. — Uncertainties listed are from fitting only.

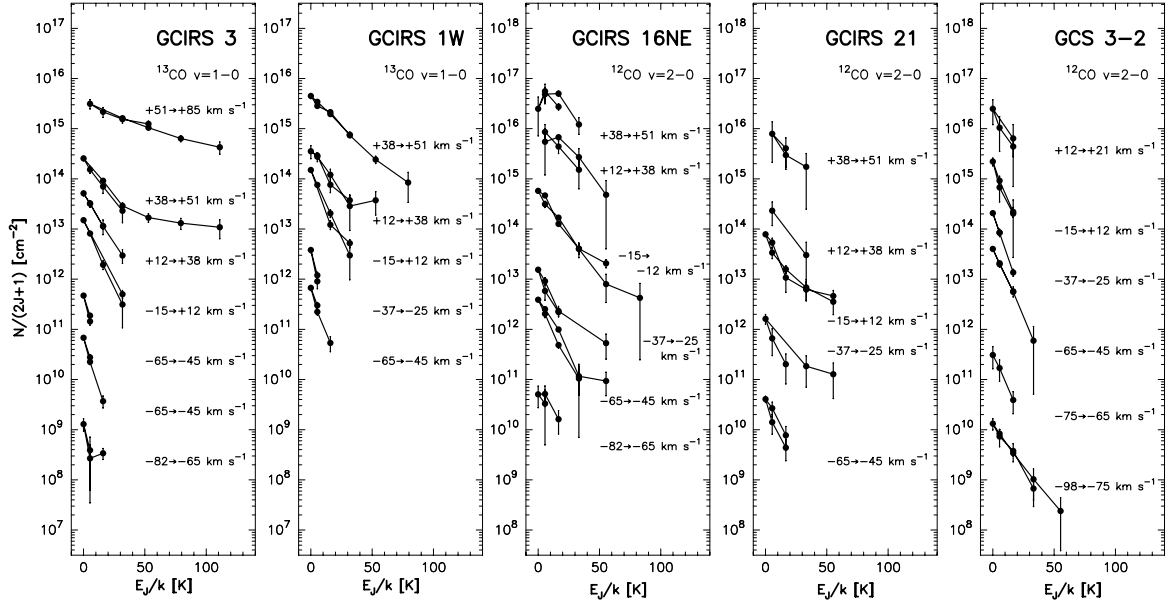


FIG. 7.— CO population diagrams for four Central Cluster sources (GCIRS 3, GCIRS 1W, GCIRS 16NE, and GCIRS 21), and the Quintuplet Cluster source GCS 3-2, calculated from the spectra in Fig. 4 and Fig. 5 for the velocity intervals highlighted in those figures. Adjacent traces are offset vertically from one another by either 1 or 2 orders of magnitudes.

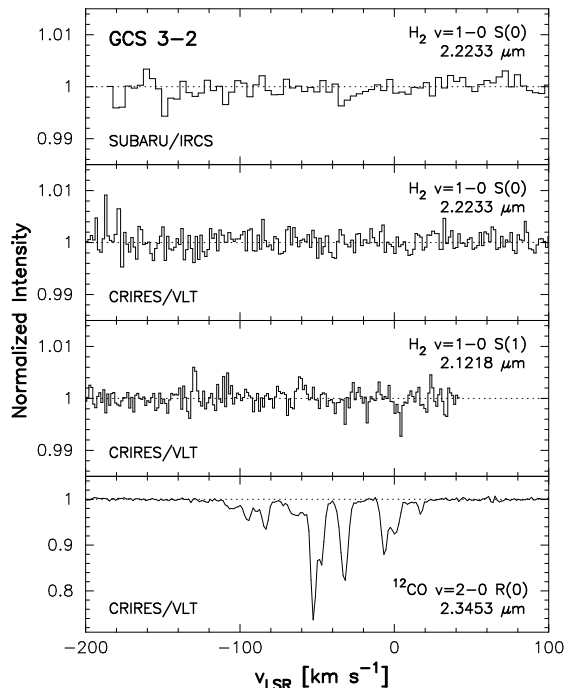


FIG. 8.— Spectra of GCS 3-2 at wavelengths of H_2 in the $2\ \mu\text{m}$ region. The spectrum of the CO $v=2-0\ R(0)$ line is shown for comparison.

related gas components. The much higher velocity gas ($\pm 300\ \text{km s}^{-1}$ or more) seen by Goicoechea et al. (2013) in the far-infrared emission lines of [N III] and [O I] was not observed in any of the $^{13}\text{CO}\ v=1-0$ lines, nor even in the wings of the saturated $^{12}\text{CO}\ v=1-0$ lines.

3.3. H_2

Figure 8 shows the spectra of GCS 3-2 obtained at the wavelengths of the $H_2\ v=1-0\ S(0)$ and $S(1)$ lines, which in absorption originate from the two lowest lying rotational levels of the molecule. Neither line was detected. The radial velocities and widths of the expected absorption features are uncertain. From the spectrum of CO (bottom of the figure) one may assume that H_2 in foreground arms would produce three narrow absorptions, each of velocity width $\sim 6\ \text{km s}^{-1}$. The upper limits on the equivalent widths of such absorption features in the observed spectrum are $2.3 \times 10^{-7}\ \mu\text{m}$ for each. For excitation temperatures of H_2 in the range 10–50 K typical of interstellar clouds, only the $J=0$ level should be significantly populated. The corresponding upper limit on the H_2 column density is $N(H_2) < 7 \times 10^{21}\ \text{cm}^{-2}$ for each arm. For a standard dust-to-gas ratio (Bohlin, Savage, & Drake 1978) and gaseous hydrogen fully molecular and not depleted by adsorption on grains each limit corresponds to $A_V < 7\ \text{mag}$. The accuracies of the limits to the extinction derived from the H_2 measurements are highly uncertain, as are any implications, because the fractions of gas in the intervening arms that are in diffuse and dense clouds are not well constrained.

4. ANALYSIS AND DISCUSSION

As described in the previous sections, the observed H_3^+ and CO absorption lines toward GCIRS 3 and

GCIRS 1W are most simply interpreted as arising in three distinct physical environments and thus at least three distinct locations along those lines of sight. The environments and likely locations are: (1) cold and mostly dense clouds in the foreground spiral and lateral arms, containing both species; (2) warm and diffuse gas within the CMZ, containing H_3^+ and relatively little CO (undetected in the overtone band of ^{12}CO nor in the fundamental band of ^{13}CO); and (3) warm and dense compact clouds in the central few parsecs of the CMZ, containing both species. In the first three subsections we use the new data and previous work by us and others to constrain the physical conditions in each of these environments. In the fourth subsection we briefly discuss possible explanations for the enhanced ionization rates in the CMZ's extended diffuse gas and in the dense gas within the central few parsecs.

4.1. Foreground Gas

The spiral arm local to the solar neighborhood, and possibly other spiral arms between the sun and the Galactic center are likely contributors to the strong absorption by CO and H_3^+ near $0\ \text{km s}^{-1}$. The sharp absorption feature at $-53\ \text{km s}^{-1}$ in both species are readily identifiable as originating in the 3 kpc arm, which was first recognized as a stream of neutral clouds by van Woerden, Rougoor, & Oort (1957) in the H I 21 cm line and then located radially by Oort et al. (1958) from the tangential point of the stream at longitude of 303° (For a recent image of it see Dame & Thaddeus 2008). Likewise, the absorption feature at $-32\ \text{km s}^{-1}$ arises in the 4 kpc arm, first identified by Menon & Ciotti (1970) via the H I line.

The weak absorption feature in CO at $-72\ \text{km s}^{-1}$ is close in velocity to an H I absorption feature at $-75\ \text{km s}^{-1}$ observed toward Sgr A by Liszt et al. (1983), who did not identify the feature with any previously known cloud. A similar kinematic component was recorded in OH 1667-MHz absorption spectrum at $-80\ \text{km s}^{-1}$ by Sandqvist (1970) on the same line of sight. It is unclear if the CO feature observed here is related to either of the above. Its presence only in low- J levels, its small angular size, and the lack of absorption features at that velocity in the H_3^+ line profiles suggest that it does not arise within the CMZ, but rather in a cold, compact, and presumably dense foreground cloud.

4.2. Warm and diffuse gas in the CMZ

4.2.1. Velocities, Densities and Temperatures

Warm and diffuse CMZ gas was discovered by Goto et al. (2002) and characterized by Oka et al. (2005), who identified it as a major constituent of the CMZ. It produces a broad and shallow swath of absorption in the $R(1,1)^l$ and $R(3,3)^l$ lines of H_3^+ , but no absorption in the $^{12}\text{CO}\ v=2-0$ or $^{13}\text{CO}\ v=1-0$ lines. It is found almost entirely at negative velocities (from $-180\ \text{km s}^{-1}$ to $+20\ \text{km s}^{-1}$); thus the gas producing it is moving outward from the center. The strength of this absorption, its presence toward stars located from the Central Cluster to as far east as the Quintuplet Cluster (Oka et al. 2005; Goto et al. 2008), and its velocity breadth suggest not only that it extends across all sightlines between the two

clusters, but also that its column length is a significant fraction of the ~ 200 pc radius of the CMZ.

The highest negative velocities observed in H_3^+ , those in excess of -100 km s^{-1} , have also been observed in the absorption and emission lines at radio wavelengths of several molecular species, e.g., CO and CS (Bally et al. 1987). It seems likely that the H_3^+ and the other molecules seen at these high velocities are physically associated. The radio lines have often been interpreted as arising near the outer edge of the CMZ (Kaifu et al. 1972; Scoville 1972; Sofue 1995), in a shell or ring-like structure (see Binney et al. 1991, for an alternative explanation). If the high velocity H_3^+ absorption also arises there, then H_3^+ absorption at lower negative velocities forms interior to it. However, the lower negative velocity gas must still be distant radially from the central few tens of parsecs, as absorption by it is observed on all sightlines from the Central Cluster to the Quintuplet Cluster.

The temperature and density of the diffuse gas can be determined from the H_3^+ level column density ratios $N(3,3)/N(1,1)$ and $N(3,3)/N(2,2)$ (Oka & Epp 2004). At low densities the former ratio is mainly temperature dependent and the latter is mainly density dependent. Fig. 9 shows temperature and density as functions of these ratios. In the velocity range $-109 \text{ km s}^{-1} \rightarrow +1 \text{ km s}^{-1}$ the 1σ lower limits of $n(3,3)/n(2,2)$ toward the two Central Cluster sources are 3.7 and 5.4, which correspond to mean temperatures near 250 K and mean densities $n \lesssim 50 \text{ cm}^{-3}$.

In Fig. 2 the spectra of GCIRS 1W show warm and diffuse gas at positive velocities as high as $+50 \text{ km s}^{-1}$ as evidenced by the weakness of the absorption in the $R(2,2)^l$ line. This positive velocity diffuse gas, previously seen by Goto et al. (2008), is not clearly present on any other Galactic center sightlines observed to date, although it may contribute to the absorption profiles seen toward GCIRS 3. Fig. 9 shows that while this gas is diffuse it is somewhat higher density than the diffuse gas on other GC sightlines.

4.2.2. Ionization Rate

The simple chemistry of H_3^+ in the diffuse interstellar medium allows one to determine the product ζL from the equation (Oka et al. 2005; Oka 2006)

$$\zeta L = 2k_e N(\text{H}_3^+)_{\text{total}} (n_C/n_H)_{\text{SV}} R_X / f(\text{H}_2), \quad (1)$$

where k_e is the rate constant for the dissociative recombination of H_3^+ on electrons, $(n_C/n_H)_{\text{SV}}$ is the carbon to hydrogen ratio in diffuse clouds in the solar vicinity, R_X is the factor increase of that ratio from the solar vicinity to the GC (due to higher metallicity in the GC), and $f(\text{H}_2) = 2n(\text{H}_2)/n_H$ is the fraction of hydrogen in molecular form. We use the value of k_e at 230 K, $8.1 \times 10^{-8} \text{ cm}^3 \text{ s}^{-1}$, calculated from Eq. (7) of McCall et al. (2004) (note that the recent experiment by Petrignani et al. (2011) implies a somewhat larger value), and $(n_C/n_H)_{\text{SV}} = 1.6 \times 10^{-4}$ (Sofia et al. 2004). We use $R_X = 3$, which appears to be conservative lower limit (Sodroski et al. 1995; Arimoto et al. 1996; Rolleston et al. 2000; Chiappini 2001; Esteban et al. 2005), and $f(\text{H}_2) = 1$. Then

$$\zeta L > (7.8 \times 10^{-11} \text{ cm}^3 \text{ s}^{-1}) N(\text{H}_3^+)_{\text{total}}.$$

The total H_3^+ column densities in the warm and diffuse gas, calculated from the sum of $N(1,1)$ and $N(3,3)$ from -180 km s^{-1} to $+20 \text{ km s}^{-1}$ in Table 2 and $N(1,0)$ in Table 4 of Goto et al. (2008) (after multiplying by 0.83 in the case of GCIRS 1W to adjust for the different velocity intervals), are $3.0 \times 10^{15} \text{ cm}^{-2}$ toward each source. The actual value may be several percent higher because the higher metastable levels such as (4,4), (5,5), (6,6) (Oka & Epp 2004) and some unstable levels such as (2,2), and (2,1) may have non-negligible populations.

We thus obtain $\zeta L > 2.3 \times 10^5 \text{ cm s}^{-1}$, which is similar to the lower limit found toward GCS 3-2 (Oka et al. 2005) and toward other stars from Sgr A* to 30 pc east (Goto et al. 2008). The limit is more than an order of magnitude higher than values in diffuse clouds in the Galactic disk $(0.5\text{--}1.9) \times 10^4 \text{ cm s}^{-1}$ (McCall et al. 2002; Indriolo et al. 2007) and more than three orders of magnitude higher than values in Galactic dense clouds (McCall et al. 1999). This may be partly attributable to the line of sight extent of diffuse gas in the CMZ being considerably longer than in Galactic diffuse clouds. However, use of the average value of ζ in Galactic diffuse clouds, $3.5 \times 10^{-16} \text{ s}^{-1}$ (Indriolo & McCall 2012), gives $L > 200 \text{ pc}$, which is comparable to the radius of the CMZ. Since it is unlikely that the warm and diffuse gas fills the entirety of the foreground CMZ, ζ is probably considerably greater than its average value in Galactic diffuse clouds.

This conclusion is strengthened by the likelihood that $f(\text{H}_2)$ is considerably less than unity in the warm and diffuse gas in the CMZ. No information about $f(\text{H}_2)$ on Central Cluster sightlines is available. Elsewhere in the CMZ recent Herschel observations have revealed strong H_2O^+ line emission towards Sgr B2 (Schilke et al. 2010) with a complex velocity profile strikingly similar to that found for H_3^+ toward 2MASS J17470898-2829561 (Geballe & Oka 2010), at a projected distance of only 17 pc from Sgr B2. This similarity indicates that the two sightlines pass through the same clouds. Models suggest that H_2O^+ can only exist in regions where $f(\text{H}_2)$ is less than 0.1, since H_2O^+ would be quickly destroyed through the reaction $\text{H}_2\text{O}^+ + \text{H}_2 \rightarrow \text{H}_3\text{O}^+$ (Gerin et al. 2010). If $f(\text{H}_2)$ smaller than 0.1 is appropriate for the sightlines toward the Central Cluster and Quintuplet sources the ionization rates there may exceed 10^{-14} s^{-1} . It would be surprising if such large amounts of H_3^+ as observed in the CMZ can be generated if $f(\text{H}_2)$ is that small. It does seem safe to conclude that $\zeta > 1 \times 10^{-15} \text{ s}^{-1}$ in the CMZ's diffuse gas.

4.3. Warm, Dense and Compact Clouds

At positive velocities the spectra of H_3^+ and ^{13}CO reveal the presence of two warm and dense clouds. The most redshifted of these, observed only toward GCIRS 3, produces broad and asymmetric absorption features in both ^{13}CO and H_3^+ . In ^{13}CO the feature extends from $+50 \text{ km s}^{-1}$ to $+85 \text{ km s}^{-1}$, with maximum absorption near $+60 \text{ km s}^{-1}$ and is observable out to $J=6$ (Fig. 4). In H_3^+ a similarly asymmetric absorption feature extends from $+40 \text{ km s}^{-1}$ to $+80 \text{ km s}^{-1}$, with maximum absorption near $+55 \text{ km s}^{-1}$, in all three lines including $R(2,2)^l$ (Fig. 2).

The other cloud produces a narrow and weak absorp-

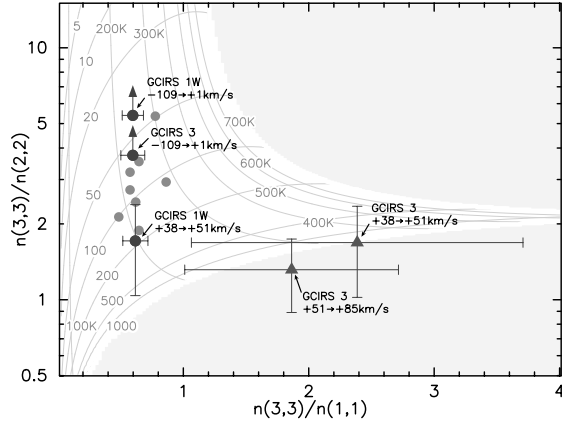


FIG. 9.— Temperature and density diagram for H_3^+ , with $n(3,3)/n(2,2)$ plotted against $n(3,3)/n(1,1)$. Dark circles for GCIRS 1W and GCIRS 3 in the velocity intervals -109 to $+1$ km s⁻¹ and for GCIRS 1W for $+38$ to $+51$ km s⁻¹ correspond to the warm and diffuse gas in the CMZ. GCIRS 1W at $+38$ to $+51$ km s⁻¹ is shown separately because that velocity interval corresponds to a detection of weak $R(2,2)^l$ line absorption; $n(3,3)/n(2,2)$ for all other points are lower limits. Gray circles denote lower limits on sightlines within 30 pc of Sgr A* from Goto et al. (2008). Filled triangles for GCIRS 3 at $+38$ to $+51$ km s⁻¹ and $+51$ to $+85$ km s⁻¹ correspond to warm, dense and compact clouds probably associated with the CND (see text).

tion (FWHM ~ 10 km s⁻¹) centered near $+45$ km s⁻¹ in ¹³CO toward both GCIRS 1W out to $J=5$ and GCIRS 3, and is detectable out to $J=6$. In the lower J levels the absorptions produced by this cloud are stronger toward GCIRS 1W than toward GCIRS 3. The presence of this cloud as a distinct entity is less obvious in the spectra of H_3^+ , which show a broad absorption centered near $+40$ km s⁻¹ toward GCIRS 1 but no clear feature toward GCIRS 3. Little or no absorption in the H_3^+ $R(2,2)^l$ line is evident toward GCIRS 1W. In the following sections we refer to the clouds producing these two velocity features as the $+60$ km s⁻¹ cloud and the $+45$ km s⁻¹ cloud.

4.3.1. Densities and Temperatures

To estimate physical conditions in the $+60$ km s⁻¹ and $+45$ km s⁻¹ clouds toward GCIRS 3, we again use the H_3^+ line ratios, after integrating the H_3^+ line strengths over the velocity ranges of the two clouds. Here we have subtracted the spectra of H_3^+ toward GCIRS 1W from those toward GCIRS 3, under the assumption that the warm diffuse gas seen toward the former source extends across the latter. The results are shown in Fig. 9. For the $+60$ km s⁻¹ cloud ($+51$ to $+85$ km s⁻¹) the data point is in a region where the inversion of the original diagram in Oka & Epp (2004) does not have a solution. We use the original diagram to obtain $T = (300 \pm 50)$ K and $n \geq 10^4$ cm⁻³. Similar results are obtained for the $+45$ km s⁻¹ cloud ($+38$ to $+51$ km s⁻¹) at GCIRS 3.

Excitation temperatures and total ¹³CO column densities in the positive velocity clouds toward GCIRS 3 and GCIRS 1W were estimated from their population diagrams in Fig. 7. The results are summarized in Table 7. A two-temperature model was used for the $+45$ km s⁻¹

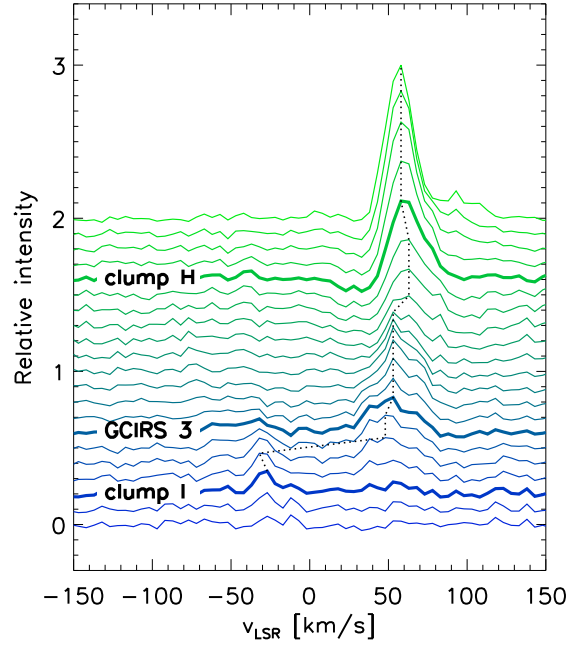


FIG. 10.— HCN $J=4-3$ emission lines (Montero-Castaño et al. 2009) extracted from the apertures between clumps H and I shown in Fig. 1. The velocity of the peak line emission is marked by a dotted line (originally published in Goto et al. 2013).

cloud toward GCIRS 3 ($+38$ to $+51$ km s⁻¹ in Fig. 7), as the level population turns over near $J=3$. Although it is likely that the CO is subthermally excited it was not possible to reproduce the observed turnover in the level populations using the radiation transfer code RADEX (Van der Tak et al. 2007). We note that the critical density for collisionally maintaining an LTE population of CO up to $J=5$ is $\sim 4 \times 10^5$ cm⁻³ (Kramer et al. 2004). Because these clouds likely exist in an intense infrared radiation field, which might assist in populating the lower rotational levels of CO, their effective “critical” densities could be somewhat less. In any event the estimates are consistent with those based on the H_3^+ lines.

4.3.2. Location

The velocity of the $+60$ km s⁻¹ cloud naively suggests that it may be associated with the well-known giant molecular cloud M-0.02-0.07, also known as the “ $+50$ km s⁻¹ cloud” (Brown & Liszt 1984). However, that cloud, which gives the strongest CO radio emission on this sightline (Oka et al. 1998), is located behind the Central Cluster, as surmised from the lack of ¹²CO $v=1-0$ absorption toward GCIRS 1W (Geballe, Baas, & Wade 1989) as well as from radio studies of NH₃ (Ho et al. 1991; Coil & Ho 2000, see their Fig. 1). Both the close proximity of GCIRS 3 to Sgr A* in the plane of the sky, suggesting that GCIRS 3 resides in the central parsec, and the requirement of a sharp edge in the cloud to provide absorption toward GCIRS 3 but not toward GCIRS 1W argue against the absorber being M-0.02-0.07.

We suggest instead that the $+60$ km s⁻¹ cloud is associated with the Galactic center’s Circumnuclear Disk (CND), as originally proposed by Geballe, Baas, & Wade (1989). The locations of the stars in the Central Cluster are compared to an

TABLE 7
TOTAL COLUMN DENSITIES OF ^{13}CO AND EXCITATION TEMPERATURE OF GALACTIC CENTER CLOUDS AT POSITIVE VELOCITIES

^{13}CO	+45 km s $^{-1}$ cloud +38 \rightarrow +51 km s $^{-1}$		+60 km s $^{-1}$ cloud +51 \rightarrow +85 km s $^{-1}$	
	N_{CO} [10^{16} cm $^{-2}$]	T_{ex} [K]	N_{CO} [10^{16} cm $^{-2}$]	T_{ex} [K]
GCIRS 3	0.8 ± 0.1	9.8 ± 1.1	—	—
GCIRS 3 (warm)	1.0 ± 0.2	50.8 ± 6.4	6.0 ± 0.6	52.8 ± 5.4
GCIRS 1W	3.2 ± 0.1	18.4 ± 0.7	—	—

NOTE. — Uncertainties listed are from fitting only.

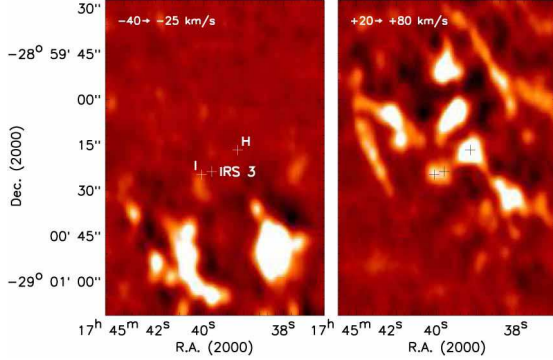


FIG. 11.— HCN $J=4-3$ maps (Montero-Castaño et al. 2009) integrated over the velocity intervals -40 to -25 km s $^{-1}$ (left) and $+20$ to $+80$ km s $^{-1}$ (right). The locations of clump H, I, and GCIRS 3 are shown by crosses.

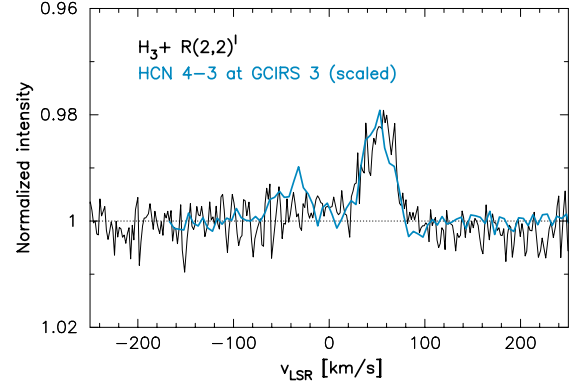


FIG. 12.— Comparison of H_3^+ $R(2,2)^l$ absorption toward GCIRS 3 (black) to HCN $J=4-3$ emission line (Montero-Castaño et al. 2009) extracted at the location of GCIRS 3 (blue, scaled to $R(2,2)^l$) (originally published in Goto et al. 2013).

HCN $J=4-3$ map of Montero-Castaño et al. (2009) in Fig. 1. GCIRS 3 coincides with an extension of the northwest portion of the CND to the east-southeast (i.e. into the interior of the CND) termed “clump I” by Montero-Castaño et al. (2009), while the line of sight to GCIRS 1W is clear. Clump I is close to Sgr A*, and thus far from the inner edge of the CND. In order to determine if this extension is related to the CND, HCN $J=4-3$ spectra were extracted along the line connecting clump H (in the main portion of the CND as seen in Fig. 1) and clump I. The spectra are shown in Fig. 10. The radial velocity at the line peak smoothly changes from $+60$ km s $^{-1}$ to $+50$ km s $^{-1}$ from clump H to the position of GCIRS 3 at the western extension of clump I, as well as steadily decreasing in intensity. Emission at this velocity disappears just beyond clump I; the intensity peak there is due to emission at -30 km s $^{-1}$. This shift in radial velocity of the peak is also visible in the velocity-integrated map of HCN $J=4-3$ in Fig. 11. Thus the western extension of clump I, which intersects the line of sight to GCIRS 3, is physically connected to clump H of the CND, rather than to the source of emission peak at clump I at -30 km s $^{-1}$, which likely is situated in the background.

The H_3^+ $R(2,2)^l$ absorption line toward GCIRS 3 is compared to HCN $J=4-3$ emission line extracted at the position of GCIRS 3 in Fig. 12. The line profiles match almost perfectly in terms of their line center velocities and widths. We conclude that the $+60$ km s $^{-1}$ absorption observed toward GCIRS 3 in ^{13}CO and H_3^+ occurs in the western extension of clump I, which is a part of the CND. The extension was not resolved by the $4''.6 \times 3''.0$ synthesized beam of the SMA (Montero-Castaño et al.

2009); thus its linear dimension is less than 0.2 pc.

It is not surprising that this gas, observed by us up to $J=6$ in ^{13}CO , is warm. The presence of high temperature gas in the CND, although not specifically on this sightline, has been known from millimeter wave spectroscopy ^{12}CO populated up to $J = 7$ (Moneti, Cernicharo, & Pardo 2001; Bradford et al. 2005), and up to $J = 24$ (Goicoechea et al. 2013)). Bradford et al. (2005), Requena-Torres et al. (2012), and Goicoechea et al. (2013) compared multiple CO rotational lines with non-LTE radiation transfer models to estimate the ambient gas density to be 10^4 – 10^5 cm $^{-3}$. Previously Christopher et al. (2005) and Montero-Castaño et al. (2009) estimated the gas density of the clumps in their HCN maps to be $> 10^8$ cm $^{-3}$, assuming the clumps are virialized. Mills et al. (2013) recently argued, however, that in the CND the effective critical density of HCN is reduced by radiative pumping in the mid-infrared in the CND, $\sim 10^4$ – 10^5 cm $^{-3}$. Our H_3^+ spectroscopy seems to be more consistent with the latter values.

The mass of the $+60$ km s $^{-1}$ cloud may be crudely estimated assuming a diameter given by the separation of GCIRS 1W and GCIRS 3 and the gas density derived from H_3^+ spectroscopy, $\sim 10^4$ cm $^{-3}$. We obtain $M \sim 4 M_\odot$. We are unable to identify the material producing the $+45$ km s $^{-1}$ feature toward GCIRS 1W and GCIRS 3 with any known cloud and do not attempt to estimate its mass.

4.3.3. Ionization Rate

For dense clouds, in which electrons are scarce and proton hop reactions from H_3^+ to CO are the main destruction channel for H_3^+ , we use the analog to Equation 1,

$$\zeta L = k_L N(\text{H}_3^+)_{\text{total}} (n_{\text{CO}}/n_{\text{H}_2})_{\text{SV}} R_X, \quad (2)$$

where the Langevin rate constant for CO, $k_L = 2 \times 10^{-9} \text{ cm}^3 \text{ s}^{-1}$ (Anicich & Huntress 1986), replaces k_e in Equation 1. For the CO to H_2 ratio we use 8×10^{-4} , the value measured by in the dense cloud in front of NGC 2024 IRS 2 by Lacy et al. (1994), and then multiply by the lower limit $R_X = 3$ in view of the higher metallicity in the GC, as discussed earlier. Using the observed total H_3^+ column density for the +60 km s^{-1} cloud toward GCIRS 3, $6 \times 10^{14} \text{ cm}^{-2}$ (the sum of the column densities in the bottom two rows in Table 2), and multiplying by 1.5 to account for destruction of H_3^+ by other dense cloud species, most notably O, we obtain $\zeta L > 1.5 \times 10^3 \text{ cm s}^{-1}$. If the path length through the +60 km s^{-1} cloud is 0.3 pc, $\zeta > 1.6 \times 10^{-15} \text{ s}^{-1}$. As in the case of the diffuse CMZ gas, this lower limit is significantly greater than mean values for dense or diffuse clouds outside of the GC.

4.4. High Ionization Rates in the CMZ

The sources of the enhanced ionization rates in the CMZ ($\zeta > 1 \times 10^{-15} \text{ s}^{-1}$ found here and also by Oka et al. (2005) and Goto et al. (2008) in the widely distributed diffuse gas, and $\zeta > 1.6 \times 10^{-15} \text{ s}^{-1}$ found here for the dense +60 km s^{-1} cloud associated with the CNB are not clearly identified. Both increased cosmic ray particle fluxes, arising from the relatively high concentration of supernova remnants in the GC, and enhanced photoionization by ultraviolet and X-ray photons from the nearby hot and luminous stars, supernova remnants, accretion disks of black holes, and ultra-hot diffuse gas are possible contributors (Crocker et al. 2011; Munro et al. 2009; Yusef-Zadeh et al. 2007).

In the CMZ ionization of hydrogen due to UV radiation would be strongly influenced by the distribution of gas and dust. For gas densities of 100 cm^{-3} or more, mean free paths for UV photons are small fractions of a parsec. The situation is different for X-rays. The X-ray photoionization cross section per hydrogen atom is $\sim 10^{-22} \text{ cm}^2$ per hydrogen atom at 1 keV (Wilms, Allen, & McCray 2000). In diffuse gas the mean free path of a 1 keV X-ray photon is a few tens of parsecs. X-ray images of the Galactic center reveal an extended diffuse component and a plethora of point sources with no individual source or group of sources that are dominant (Baganoff et al. 2003; Munro et al. 2009). Thus it would not be surprising if the ionization rate, even if enhanced due to X-rays, or due to cosmic ray particles, were roughly constant on widely spaced sightlines through the extended warm and diffuse gas in the CMZ, as seems to be the case

(Oka et al. 2005; Goto et al. 2008, 2011).

On the other hand, the high ionization rate measured in the +60 km s^{-1} cloud, which is located close to the Central Cluster and to Sgr A*, might be attributed in part to recent flares of local X-ray sources such as Sgr A* itself, or possibly to UV ionization from the multitude of hot stars in the nearby Central Cluster. For more detailed discussion of ionization rates in the central few pc of the Galaxy, see Goto et al. (2013), who estimated X-ray and cosmic ray ionization rates based on X-ray and γ -ray observations near Sgr A*.

5. CONCLUSION

The basic physical properties of the gas in the Central Molecular Zone of the Galaxy have been quantified on sightlines toward infrared stars in the Central Cluster that are within a few tenths of a parsec of Sgr A*, using new infrared absorption spectra of H_3^+ and CO. Two types of gaseous environments within the CMZ have been identified on these sightlines: (1) warm ($200 \text{ K} < T < 300 \text{ K}$) and diffuse ($n \leq 100 \text{ cm}^{-3}$) gas with velocities in the range -180 km s^{-1} to $+20 \text{ km s}^{-1}$ occupying a significant fraction of the outer portion of the CMZ; (2) warm ($T \sim 300 \text{ K}$) and dense ($n \geq 10^4 \text{ cm}^{-3}$) gas probably belonging to an inward extension of the 1.5 pc radius Circumnuclear Disk that is on the line of sight to GCIRS 3. In addition, cold dense and diffuse gas located in foreground spiral and lateral arms has been observed on these sightlines.

From the observed total column densities of H_3^+ , products of ionization rate ζ and pathlength L have been determined to be $\zeta L > 2.3 \times 10^5 \text{ cm s}^{-1}$ and $\zeta L > 1.5 \times 10^3 \text{ cm s}^{-1}$, respectively, for the above diffuse and dense CMZ gas. Although separation of ζ and L is difficult, the large values of their products indicate ionization rates ($\zeta > 10^{-15} \text{ s}^{-1}$) in both environments, and large path lengths ($L > 30 \text{ pc}$) in the diffuse gas of the CMZ.

We are grateful to the staffs of the VLT and the Subaru Telescope for valuable assistance in obtaining these data. We thank the anonymous referee for constructive suggestions that markedly improved the paper. We also thank María Montero-Castaño for providing HCN $J=4-3$ map in machine-readable form. This research has made use of the SIMBAD database, operated at CDS, Strasbourg, France. The image of the Central Cluster was obtained through the ESO Science Archive Facility. T. O. is supported by NSF grant AST 1109014. M. G. is supported by DFG grant GO 1927/3-1. T. R. G.'s research is supported by the Gemini Observatory, which is operated by the Association of Universities for Research in Astronomy, Inc., on behalf of the international Gemini partnership of Argentina, Australia, Brazil, Canada, Chile, the United Kingdom, and the United States of America. We appreciate the hospitality of Chilean and Hawaiian communities, who made this research possible.

REFERENCES

- An, D., Ramírez, S. V., Sellgren, K., Arendt, R. G., Adwin Boogert, A. C., Robitaille, T. P., Schultheis, M., et al. 2011, *ApJ*, 736, 133
 Anicich, V. G., & Huntress, W. T., Jr. 1986, *ApJS*, 62, 553
 Arimoto, N., Sofue, Y., & Tsujimoto, T. 1996, *PASJ*, 48, 275

- Baganoff, F. K., Maeda, Y., Morris, M., Bautz, M. W., Brandt, W. N., Cui, W., Doty, J. P., Feigelson, E. D., Garmire, G. P., Pravdo, S. H., Ricker, G. R., & Townsley, L. K. 2003, *ApJ*, 591, 891
- Bally, J., Stark, A. A., Wilson, R. W., & Henkel, C. 1987, *ApJS*, 65, 13
- Bartko, H., Martins, F., Trippe, S., Fritz, T. K., Genzel, R., Ott, T., Eisenhauer, F., Gillessen, S., Paumard, T., Alexander, T., Dodds-Eden, K., Gerhard, O., Levin, Y., Mascetti, L., Nayakshin, S., Perets, H. B., Perrin, G., Pfuhl, O., Reid, M. J., Rouan, D., Zilka, M., & Sternberg, A. 2010, *ApJ*, 708, 834
- Binney, J., Gerhard, O. E., Stark, A. A., Bally, J., & Uchida, K. I. 1991, *MNRAS*, 252, 210
- Bohlin, R. C., Savage, B. D., & Drake, J. F. 1978, *ApJ*, 224, 132
- Bonnet et al. 2004, *The ESO Messenger*, 117, 17
- Bradford, C. M., Stacey, G. J., Nikola, T., Bolatto, A. D., Jackson, J. M., Savage, M. L., & Davidson, J. A. 2005, *ApJ*, 623, 866
- Brown, R. L., & Liszt, H. S. 1984, *ARA&A*, 22, 223
- Chackerian, Jr., C., & Tipping, R. H. 1983, *J. Molec. Spectrosc.*, 99, 431
- Chiappini, C., Matteucci, F., & Romano, D. 2001, *ApJ*, 554, 1044
- Christopher, M. H., Scoville, N. Z., Stolovy, S. R., & Yun, M. S. 2005, *ApJ*, 622, 346
- Coil, A. L., & Ho, P. T. P. 2000, *ApJ*, 533, 245
- Crocker, R. M., Jones, D. I., Aharonian, F., Law, C. J., Melia, F., Oka, T., & Ott, J. 2011, *MNRAS*, 413, 763
- Dame, T. M., & Thaddeus, P. 2008, *ApJ*, 683, L143
- Eisenhauer, F., Schödel, R., Genzel, R., Ott, T., Tecza, M., Abuter, R., Eckart, A., & Alexander, T. 2003, *ApJ*, 597, L121
- Esteban, C., García-Rojas, J., Peimbert, M., Peimbert, A., Ruiz, M. T., Rodríguez, M., & Carigi, L. 2005, *ApJ*, 618, L95
- Geballe, T. R., & Oka, T. 1996, *Nature*, 384, 334
- Geballe, T. R., Baas, F., & Wade, R. 1989, *A&A*, 208, 255
- Geballe, T. R. & Oka, T. 2010, *ApJ*, 709, L70
- Geballe, T. R., McCall, B. J., Hinkle, K. H., & Oka, T. 1999, *ApJ*, 510, 251
- Genzel, R. & Townes, C. H. 1987, *ARA&A*, 25, 377
- Gerin, M., de Luca, M., Black, J., et al. 2010, *A&A*, 518, L110
- Ghez, A. M., Salim, S., Weinberg, N. N., Lu, J. R., Do, T., Dunn, J. K., Matthews, K., Morris, M. R., Yelda, S., Becklin, E. E., Kremenek, T., Milosavljevic, M., & Naiman, J. 2008, *ApJ*, 689, 1044
- Goicoechea, J. R., Etxaluze, M., Cernicharo, J., Gerin, M., Neufeld, D. A., Contursi, A., Bell, T. A., de Luca, M., Encarnaz, P., Indriolo, N., Lis, D. C., Polehampton, E. T., & Sonnentrucker, P. 2013, *ApJ*, 769, L13
- Goto, M., McCall, B. J., Geballe, T. R., Usuda, T., Kobayashi, N., Terada, H., & Oka, T. 2002, *PASJ*, 54, 951
- Goto, M., Usuda, T., Nagata, T., Geballe, T. R., McCall, B. J., Indriolo, N., Suto, H., Henning, Th., Morong, C. P., & Oka, T. 2008, *ApJ*, 688, 306
- Goto, M., Usuda, T., Geballe, T. R., Indriolo, N., McCall, B. J., Henning, Th., & Oka, T. 2011, *PASJ*, 63, L13
- Goto, M., Indriolo, N., Geballe, T. R., & Usuda, T. 2013, *J. Phys. Chem.*, 117, 9919
- Güsten, R., Walmsley, C. M., & Pauls, T. 1981, *A&A*, 103, 197
- Ho, L. C., Szczepanski, J. C., Ho, P. T. P., Jackson, J. M., & Armstrong, J. T., 1991, *Atoms, ions, and molecules: New Results in spectral line astrophysics*, ASP Conference Series (ASP: San Francisco), 16, p 177
- Immer, K., Schuller, F., Omont, A., & Menten, K. M. 2012, *A&A*, 537, 121
- Indriolo, N., Geballe, T. R., Oka, T., & McCall, B. J. 2007, *ApJ*, 671, 1736
- Indriolo, N., & McCall, B. J. 2012, *ApJ*, 745, 91
- Kaifu, N., Kato, T., & Iguchi, T. 1972, *Nature Phys. Sci.*, 238, 105
- Käuf, H. U., et al. 2004, *Proc. SPIE*, 5492, 1218
- Kramer, C., Jakob, H., Mookerjee, B., Schneider, N., Brüll, M., Stutzki, J. 2004, *A&A*, 424, 887
- Lacy, J. H., Knacke, R., Geballe, R., & Tokunaga, A. T. 1994, *ApJ*, 428, L69
- Lazio, T. J. W., & Cordes, J. M. 1998, *ApJ*, 505, 715
- Lis, D. C., Serabyn, E., Zylka, R., & Li, Y. 2001, *ApJ*, 550, 761
- Liszt, H. S., van der Hulst, J. M., Burton, W. B., & Ondrechen, M. P. 1983, *A&A*, 126, 341
- Lord, S. D. 1992, *A New Software Tool for Computing Earth's Atmosphere Transmissions of Near- and Far-Infrared Radiation*, NASA Technical Memoir 103957 (Moffett Field, CA: NASA Ames Research Center)
- McCall, B. J., Hinkle, K. H., Geballe, T. R., Moriarty-Schieven, G. H., Evans, N. J., II, Kawaguchi, K., Takano, S., Smith, V. V., & Oka, T. 2002, *ApJ*, 567, 391
- McCall, B. J. et al. 2004, *Phys. Rev. A*, 70, 052716
- McCall, B. J., Geballe, T. R., Hinkle, K. H., & Oka, T. 1999, *ApJ*, 522, 338
- Mills, E. A. C., Güsten, R., Requena-Torres, M. A., & Morris, M. R. 2013, *ApJ*, 779, 47
- Menon, T. K., & Ciotti, J. E. 1970, *Nature*, 227, 579
- Moneti, A., Cernicharo, J., & Pardo, J. R., 2001, *ApJ*, 549, L203
- Montero-Castaño, M., Herrnstein, R. M., & Ho, P. T. P. 2009, *ApJ*, 695, 1477
- Morris, M., Polish, N., Zuckerman, B., & Kaifu, N. 1983, *AJ*, 88, 1228
- Morris, M., & Serabyn, E. 1996, *ARA&A*, 34, 645
- Moultaka, J., Eckart, A., & Schödel, R. 2009, *ApJ*, 703, 1635
- Muno, M. P., Bauer, F. E., Baganoff, F. K., Bandyopadhyay, R. M., Bower, G. C., Brandt, W. N., Broos, P. S., Cotera, A., Eikenberry, S. S., Garmire, G. P., Hyman, S. D., Kassim, N. E., Lang, C. C., Lazio, T. J. W., Law, C., Mauerhan, J. C., Morris, M. R., Nagata, T., Nishiyama, S., Park, S., Ramirez, S. V., Stolovy, S. R., Wijnands, R., Wang, Q. D., Wang, Z., & Yusef-Zadeh, F. 2009, *ApJS*, 181, 110
- Neale, L., Miller, S., & Tennyson, J. 1996, *ApJ*, 464, 516
- Neufeld, D. A. 2012, *ApJ*, 749, 125
- Oka, T. 2006, *Proc. Natl. Acad. Sci. USA*, 103, 12235
- Oka, T., & Epp, E. 2004, *ApJ*, 613, 349
- Oka, T., Geballe, T. R., Goto, M., Usuda, T., & McCall, B. J. 2005, *ApJ*, 632, 882
- Oka, T., Hasegawa, T., Sato, F., Tsuboi, M., & Miyazaki, A. 1998, *ApJS*, 118, 455
- Oort, J. H., Kerr, F. J., & Westerhout, G. 1958, *MNRAS*, 118, 379
- Pan, F.-S., & Oka, T. 1986, *ApJ*, 305, 518
- Paumard, T., Genzel, R., Maillard, J.-P., Ott, T., Morris, M. R., Eisenhauer, F., & Abuter, R. 2004, in *Young Local Universe*, ed. A. Chalabaev et al. (Paris: Éditions Frontières), 377
- Paumard, T., Genzel, R., Martins, F., Nayakshin, S., Beloborodov, A. M., Levin, Y., Trippe, S., Eisenhauer, F., Ott, T., Gillessen, S., Abuter, R., Cuadra, J., Alexander, T., & Sternberg, A. 2006, *ApJ*, 643, 1011
- Petrignani, A., Altevogt, S., Berg, M. H., Bing, D., Grieser, M., Hoffmann, J., Jordon-Thaden, B., Krantz, C., Mendes, M. B., Novotný, Oldřich, Novotný, S., Orlov, D. A., Repnow, R., Sorg, T., Stützel, J., Wolf, A., Buhr, H., Kreckel, H., Kokoouline, V., & Greene, C. H. 2011, *Phys. Rev. A*, 83, 032711
- Pierce-Price, D., Richer, J. S., Greaves, J. S., et al. 2000, *ApJ*, 545, L121
- Requena-Torres, M. A., Güsten, R., Weiß, A., Harris, A. I., Martín-Pintado, J., Stutzki, J., Klein, B., Heyminck, S., & Risacher, C. 2012, *A&A*, 542, L21
- Rolleston, W. R. J., Smartt, S. J., Dufton, P. L., & Ryans, R. S. I. 2000, *A&A*, 363, 537
- Sandqvist, A. 1970, *AJ*, 75, 135
- Schilke, P., Comito, C., Müller, H. et al. 2010, *A&A*, 521, L11
- Scoville, N. Z. 1972, *ApJ*, 175, L127
- Serabyn, E., & Güsten, R. 1986, *A&A*, 161, 334
- Sodroski, T. J., Odegard, N., Dwek, E., Hauser, M. G., Franz, B. A., Freedman, I., Kelsall, T., Wall, W. F., Berriman, G. B., Odenwald, S. F., Bennett, C., Reach, W. T., & Weiland, J. L. 1995, *ApJ*, 452, 262
- Sofia, U. J., Lauroesch, J. T., Meyer, D. M., & Cartledge, S. I. B. 2004, *ApJ*, 605, 272
- Sofue, Y. 1995, *PASJ*, 47, 551
- Sutton, E. C., Danchi, W. C., Jaminet, P. A., & Masson, C. R. 1990, *ApJ*, 348, 503
- van der Tak, F. F. S., Black, J. H., Schöier, F. L., Jansen, D. J., van Dishoeck, E. F. 2007, *A&A*, 468, 627
- van Woerden, H., Rougoor, G. W., & Oort, J. H. 1957, *Comptes Rendus*, 244, 1691
- Wilms, J., Allen, A., & McCray, R., 2000, *ApJ*, 542, 914
- Yusef-Zadeh, F., Muno, M., Wardle, M., & Lis, D. C. 2007, *ApJ*, 656, 847
- Yusef-Zadeh, F., Wardle, M., & Roy, S. 2007, *ApJ*, 665, L123
- Zhao, J., Morris, M. R., Goss, W. M., & An, T. 2009, *ApJ*, 699, 186
- Zou, Q., & Varanasi, P. 2002, *J. Quant. Spectrosc. Rad. Transf.*, 75, 63